PHYSICS OF PLASMAS **22**, 102515 (2015)

Verification of nonlinear particle simulation of radio frequency waves in tokamak

A. Kuley,[1,a)] Z. Lin,[1] J. Bao,[1,2] X. S. Wei,[3] Y. Xiao,[3] W. Zhang,[4] G. Y. Sun,[5] and N. J. Fisch[6,7]
[1]*Department of Physics and Astronomy, University of California Irvine, California 92697, USA*
[2]*Fusion Simulation Center, Peking University, Beijing 100871, China*
[3]*Institute for Fusion Theory and Simulation, Zhejiang University, Hangzhou 310027, China*
[4]*Institute of Physics, Chinese Academy of Sciences, Beijing 100190, China*
[5]*Department of Physics, Institute of Theoretical Physics and Astrophysics, Xiamen University, Xiamen 361005, China*
[6]*Department of Astrophysical Sciences, Princeton University, Princeton, New Jersey 08540, USA*
[7]*Princeton Plasma Physics Laboratory, Princeton, New Jersey 08543, USA*

(Received 21 July 2015; accepted 13 October 2015; published online 27 October 2015)

Nonlinear simulation model for radio frequency waves in fusion plasmas has been developed and verified using fully kinetic ion and drift kinetic electron. Ion cyclotron motion in the toroidal geometry is implemented using Boris push in the Boozer coordinates. Linear dispersion relation and nonlinear particle trapping are verified for the lower hybrid wave and ion Bernstein wave (IBW). Parametric decay instability is observed where a large amplitude pump wave decays into an IBW sideband and an ion cyclotron quasimode (ICQM). The ICQM induces an ion perpendicular heating, with a heating rate proportional to the pump wave intensity. *© 2015 AIP Publishing LLC.* [http://dx.doi.org/10.1063/1.4934606]

I. INTRODUCTION

Magnetic fusion devices rely on radio frequency (RF) waves for driving current and heating plasmas, ever since it was predicted that the power dissipated by high phase velocity waves could be much smaller than previously thought.[1] There are now many methods of current drive considered in present-day tokamaks[2–4] and for future burning plasma experiments such as ITER.[5] The linear theory of RF waves using eigenvalue solvers (full wave method), such as AORSA,[6] TORIC,[7] and WKB method,[8,9] is widely used to explain many RF phenomena in experiments. However, there are important situations when linear theory fails and nonlinear phenomena, such as ponderomotive effects and parametric decay instability (PDI), become important. For example, the density threshold[10–12] associated with the nonlinear RF plasma interaction cannot be captured either in full wave or WKB method. The presence of PDIs, density threshold, and plasma rotation induced by nonlinear RF effects has been observed in several fusion devices, including DIII-D,[13] Alcator C-Mod,[10,14] HT-7,[15] NSTX,[16] FTU,[12] ASDEX,[17] JT-60,[18] EAST,[19] and JET.[11] Nonlinear physics of the RF waves has been studied theoretically[20–23] and numerically in slab or cylinder geometries with particle codes such as GeFi,[24] Vorpal,[25,26] and G-gauge.[27] However, the RF propagation, spectral evolution, mode conversion, and nonlinear interactions in fusion plasmas all depend on the toroidal geometry and equilibrium.

Thus, given the importance of RF for steady state operation, instability control, and requisite central heating in burning plasmas, we are developing a global nonlinear toroidal particle simulation model to study the nonlinear physics associated with RF heating and current drive using the gyrokinetic toroidal code (GTC).[28] GTC has been verified for RF waves,[29,30] energetic particle driven Alfven eigenmodes,[31–33] microturbulence,[34] and macroscopic magnetohydrodynamic (MHD) modes driven by pressure gradients and equilibrium currents.[35,36] The principle advantage of the initial value approach in GTC simulation is that it retains all the nonlinearities and other physical properties (all harmonics, finite Larmor radius effects, etc.) of the RF waves in the realistic toroidal geometry. As a important step in developing this nonlinear toroidal particle simulation model, in this paper, we have extended our fully kinetic ion simulation model from cylindrical geometry to the toroidal geometry.[29,37] Most recently, GTC has been verified for the linear and nonlinear electromagnetic simulation of lower hybrid wave (LHW). The LHW propagation, mode conversion, and absorption have been simulated using fluid ion and drift kinetic electron in the toroidal geometry.[38,39] Further developments of this electromagnetic model will enable us to analyze the nonlinear physics such as PDIs, ponderomotive effects, rf sheath, pinching effects, density threshold, and improvement of the accessibility window for RF wave penetration in the tokamak edge as well as its propagation to the core region.

In this paper, we have implemented ion cyclotron motion in magnetic coordinates and verified linear physics and nonlinear particle trapping for electrostatic LHW, and ion Bernstein wave (IBW) using fully kinetic ion and drift kinetic electron. We have also carried out simulations of three wave coupling in the ion cyclotron heating regime, in which the pump wave decays into an IBW sideband and an ion cyclotron quasimode (ICQM). When the frequency matching condition is satisfied, the quasimode is strongly damped on the ion, and the ion heating takes place only in the perpendicular direction. This quasimode induced ion heating rate is proportional to the intensity of the pump wave.

[a)] Electronic mail: akuley@uci.edu

This article is copyrighted as indicated in the article. Reuse of AIP content is subject to the terms at: http://scitation.aip.org/termsconditions. Downloaded to IP: 71.168.238.172 On: Tue, 27 Oct 2015 15:40:32

The paper is organized as follows: the physics model of fully kinetic ion and drift kinetic electron in toroidal geometry is described in Sec. II. Section III presents the linear verification of the GTC simulation of the electrostatic normal modes in uniform plasmas and nonlinear wave trapping of electron. Sec. IV describes the nonlinear ion heating due to PDI, and Section V summarizes the overall work.

II. PHYSICS MODEL IN TOROIDAL GEOMETRY

The physics model for the fully kinetic ion, drift kinetic electron dynamics, and the numerical methods associated with the time advancement of the physical quantities (ion position, electron guiding center, particle weight, electric field, etc.) is described below.

A. Physics model

1. Coordinate system

In GTC, we use toroidal magnetic coordinates (ψ, θ, ζ) to represent the electromagnetic fields and the plasma profile in the closed flux surface, where ψ is the poloidal flux function, θ and ζ are the poloidal and toroidal angle, respectively. The contravariant representation of the magnetic field is[40]

$$\vec{B} = g\nabla\zeta + I\nabla\theta, \tag{1}$$

covariant representation is

$$\vec{B} = q\nabla\psi \times \nabla\theta - \nabla\psi \times \nabla\zeta, \tag{2}$$

and the Jacobian of this magnetic toroidal system can be written as

$$J^{-1} = \nabla\psi \cdot \nabla\theta \times \nabla\zeta = \frac{B^2}{gq + I}. \tag{3}$$

Although GTC is capable of general toroidal geometry,[41] we consider a concentric cross-section tokamak in this paper. The radial coordinate ψ is simplified as the minor radius r. The toroidal coordinate system relates to the standard Cartesian system as follows [cf. Fig. 1]:

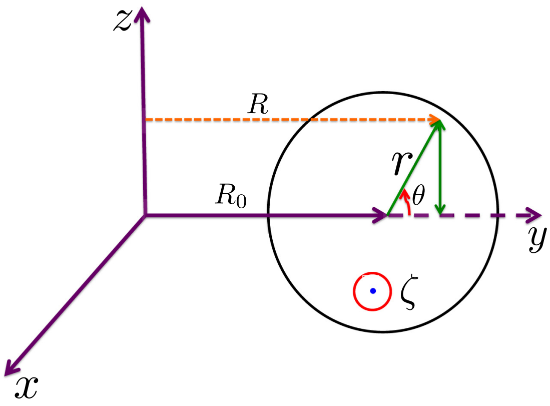

FIG. 1. Schematic diagram of the coordinates of a concentric cross section tokamak.

$$\begin{aligned} x &= (R_0 + r\cos\theta)\cos\zeta, \\ y &= -(R_0 + r\cos\theta)\sin\zeta, \\ z &= r\sin\theta. \end{aligned} \tag{4}$$

By defining a covariant basis $\vec{e}_\psi = \partial_\psi \vec{r}$, $\vec{e}_\theta = \partial_\theta \vec{r}$, $\vec{e}_\zeta = \partial_\zeta \vec{r}$ and contravariant basis $\vec{e}^{\,\psi} = \nabla\psi$, $\vec{e}^{\,\theta} = \nabla\theta$, $\vec{e}^{\,\zeta} = \nabla\zeta$, the velocity and the electric field can be written as

$$\vec{v} = v^\psi \vec{e}_\psi + v^\theta \vec{e}_\theta + v^\zeta \vec{e}_\zeta, \tag{5}$$

$$\vec{E} = -\nabla\phi = -\left[\frac{\partial\phi}{\partial\psi}\nabla\psi + \frac{\partial\phi}{\partial\theta}\nabla\theta + \frac{\partial\phi}{\partial\zeta}\nabla\zeta\right], \tag{6}$$

where

$$\begin{aligned} v^\psi &= \dot{\psi}, \quad v^\theta = \dot{\theta}, \quad v^\zeta = \dot{\zeta} r\cos\theta/(R_0 + r\cos\theta), \\ \vec{e}_\psi &= [\cos\theta\cos\zeta\hat{x} - \cos\theta\sin\zeta\hat{y} + \sin\theta\hat{z}](\partial r/\partial\psi), \\ \vec{e}_\theta &= -r\sin\theta\cos\zeta\hat{x} + r\sin\theta\sin\zeta\hat{y} + r\cos\theta\hat{z}, \\ \vec{e}_\zeta &= -(R_0 + r\cos\theta)\sin\zeta\hat{x} - (R_0 + r\cos\theta)\cos\zeta\hat{y} \\ \psi(r) &= \int_0^r (r/q)dr. \end{aligned} \tag{7}$$

2. Ion dynamics

Ion dynamics is described by the six dimensional Vlasov equation

$$\left[\frac{\partial}{\partial t} + \vec{v}\cdot\nabla + \frac{Z_i}{m_i}\left(\vec{E} + \vec{v}\times\vec{B}\right)\cdot\frac{\partial}{\partial\vec{v}}\right]f_i = 0, \tag{8}$$

where f_i is the ion distribution function, Z_i is the ion charge, and m_i is the ion mass.

The evolution of the ion distribution function f_i can be described by the Newtonian equation of motion in the presence of self-consistent electromagnetic field as follows:

$$\frac{d}{dt}\vec{r} = \vec{v}, \qquad \frac{d}{dt}\vec{v} = \frac{Z_i}{m_i}\left[\vec{E} + \vec{v}\times\vec{B}\right]. \tag{9}$$

In our simulation, we compute the marker particle trajectory [Eq. (9)] by the time centered Boris push method,[29,42,43] as discussed Section II B.

In our GTC simulation, we have implemented both perturbative (δf) and non-perturbative (full-f) methods. We use (δf_i) method to reduce the particle noise. Now, we decompose the distribution function (f_i) into its equilibrium (f_{0i}) and perturb part (δf_i), i.e., $f_i = f_{0i} + \delta f_i$. The perturbed density for ion is defined as the fluid moment of ion distribution function, $\delta n_i = \int \delta f_i d^3 v$. By defining the particle weight $w_i = \delta f_i / f_i$, we can rewrite the Vlasov equation for Maxwellian ion with uniform temperature T_i and uniform density as follows:

$$\frac{d}{dt}w_i = -\frac{Z_i}{T_i}(1 - w_i)\left[\frac{\partial\phi}{\partial\psi}v^\psi + \frac{\partial\phi}{\partial\theta}v^\theta + \frac{\partial\phi}{\partial\zeta}v^\zeta\right]. \tag{10}$$

3. Electron dynamics

Electron dynamics is described by the five-dimensional drift kinetic equation

This article is copyrighted as indicated in the article. Reuse of AIP content is subject to the terms at: http://scitation.aip.org/termsconditions. Downloaded to IP: 71.168.238.172 On: Tue, 27 Oct 2015 15:40:32

$$\left[\frac{\partial}{\partial t}+\dot{\vec{X}}\cdot\nabla+\dot{v}_\parallel\frac{\partial}{\partial v_\parallel}\right]f_e\left(\vec{X},v_\parallel,\mu,t\right)=0, \tag{11}$$

where f_e is the guiding center distribution function, $\vec{X}(\psi,\theta,\zeta)$ is the guiding center position, μ is the magnetic moment, and $v_\parallel$ is the parallel velocity. The evolution of the electron distribution function can be described by the following equations of guiding center motion:[44]

$$\begin{aligned}\dot{\vec{X}}&=v_\parallel\hat{b}+\vec{v}_E+\vec{v}_c+\vec{v}_g,\\ \dot{v}_\parallel&=-\frac{1}{m_e}\frac{\vec{B}^*}{B}\cdot(\mu\nabla B-e\nabla\phi),\end{aligned} \tag{12}$$

where $\vec{B}^*=\vec{B}+Bv_\parallel/\omega_{ce}\nabla\times\hat{b}$ and $\mu=m_ev_\perp^2/2B$. The $\vec{E}\times\vec{B}$ drift velocity $\vec{v}_E$, the grad-B drift velocity $\vec{v}_g$, and curvature drift velocity $\vec{v}_c$ are given by

$$\begin{aligned}\vec{v}_E&=\frac{c\hat{b}\times\nabla\phi}{B},\\ \vec{v}_g&=\frac{\mu}{m\omega_{ce}}\hat{b}\times\nabla B,\\ \vec{v}_c&=\frac{v_\parallel^2}{\omega_{ce}}\nabla\times\hat{b}.\end{aligned} \tag{13}$$

This electron model is suitable for the dynamics with the wave frequency $\omega\ll\omega_{ce}$ and $k_\perp\rho_e\ll 1$, where ω_{ce} is the electron cyclotron frequency and ρ_e is the electron gyro radius. Electron dynamics are described by conventional Runge-Kutta (RK) method. The perturbed density for electron also can be found from the fluid moment of electron distribution function, $\delta n_e=\int\delta f_e d^3v$. The weight equation for electron can be written as

$$\frac{d}{dt}w_e=(1-w_e)\left[-e\frac{\vec{B}^*}{B_0}\cdot\nabla\phi\frac{1}{m_e}\frac{1}{f_{0e}}\frac{\partial f_{0e}}{\partial v_\parallel}\right], \tag{14}$$

where $w_e=\delta f_e/f_e$ and $f_e=f_{0e}+\delta f_e$. f_{0e} and δf_e are the equilibrium and perturbed distribution function, respectively. Simulation related to nonuniform plasma density and temperature will be reported in future work.

4. Field equation

This paper describes the electrostatic model of fully kinetic ion and drift kinetic electron. Most recently Bao *et al.*[38] have formulated the electromagnetic description of this model. The electrostatic potential can be calculated from the Poisson's equation

$$\nabla_\perp\cdot\left[\left(1+\frac{\omega_p^2}{\omega_c^2}\right)\nabla_\perp\phi\right]=-4\pi(Z_i\delta n_i-e\delta n_e). \tag{15}$$

Here, we consider the fact that the perpendicular wavelength is much shorter than the parallel wavelength to suppress the high frequency electron plasma oscillation along the magnetic field line. The second term on the left hand side corresponds to the electron density due to its perpendicular polarization drift. For an axisymmetric system, the perpendicular Laplacian can be explicitly expressed as[41]

$$\begin{aligned}\nabla_\perp^2&=g^{\psi\psi}\frac{\partial^2}{\partial\psi^2}+2g^{\psi\theta}\frac{\partial^2}{\partial\psi\partial\theta_0}+\left(g^{\theta\theta}+g^{\zeta\zeta}/q^2\right)\frac{\partial^2}{\partial\theta_0^2}\\ &\quad+\frac{1}{J}\left(\frac{\partial Jg^{\psi\psi}}{\partial\psi}+\frac{\partial Jg^{\psi\theta}}{\partial\theta_0}\right)\frac{\partial}{\partial\psi}\\ &\quad+\frac{1}{J}\left(\frac{\partial Jg^{\psi\theta}}{\partial\psi}+\frac{\partial Jg^{\theta\theta}}{\partial\theta_0}\right)\frac{\partial}{\partial\theta_0},\end{aligned} \tag{16}$$

where $\theta_0=\theta-\zeta/q$ and $\zeta_0=\zeta$. In GTC, we used the field aligned coordinates (ψ,θ_0,ζ_0), for reducing the number of parallel grids. And, we use the B-spline representation of the magnetic field, which provides a transformation $R=R(\psi,\theta)$ and $Z=Z(\psi,\theta)$, where (R,Z,ζ) are the cylindrical coordinates. We define the contravariant geometric tensor $g^{\xi^\alpha\xi^\beta}=\nabla\xi^\alpha\cdot\nabla\xi^\beta$, $(\xi^1,\xi^2,\xi^3)=(\psi,\theta,\zeta)$. The covariant geometric tensor $g_{\xi^\alpha\xi^\beta}$ can be expressed as

$$\begin{aligned}g_{\psi\psi}&=\left(\frac{\partial R}{\partial\psi}\right)^2+\left(\frac{\partial Z}{\partial\psi}\right)^2,\\ g_{\theta\theta}&=\left(\frac{\partial R}{\partial\theta}\right)^2+\left(\frac{\partial Z}{\partial\theta}\right)^2,\\ g_{\psi\theta}&=\frac{\partial R}{\partial\psi}\frac{\partial R}{\partial\theta}+\frac{\partial Z}{\partial\psi}\frac{\partial Z}{\partial\theta},\end{aligned} \tag{17}$$

and $g_{\psi\theta}=g_{\theta\psi}, g_{\zeta\zeta}=R^2=(R_0+r\cos\theta)^2$ for concentric cross-section tokamak, where R_0 is the major radius of the tokamak.

B. Boris push for ion dynamics

The efficiency of particle simulation is strongly dependent on the particle pusher. Boris scheme is the most widely used orbit integrator in explicit particle-in-cell (PIC) simulation of plasmas. Here, we have extended our Boris push scheme from cylindrical geometry to toroidal geometry.[29] This scheme offers second order accuracy while requiring only one force (or field) evaluation per step. The interplay between the PIC cycle and the Boris scheme is schematically represented in Fig. 2. At the beginning of each cycle, the position of the particles and their time centered velocity $\vec{v}(t-1/2)$, weight $w_i(t)$, and the grid based electromagnetic fields $\vec{E}(t),\vec{B}(t)$ are given.

In the first step, we add the first half of the electric field acceleration to the velocity $\vec{v}(t-1/2)$ to obtain the velocity at the particle position $\vec{r}(t)$ as follows:

$$\vec{u}(t)=\vec{v}(t-1/2)+\frac{Z_i}{m_i}\frac{\Delta t}{2}\vec{E}(t). \tag{18}$$

One may write the components of velocity at particle position $\vec{r}(t)$ as

$$\begin{aligned}u^{\alpha-}(t)&=\sum_{\beta=\psi,\theta,\zeta}v^\beta(t-1/2)\vec{e}_\beta(t-1/2)\cdot\nabla\alpha(t)\\ &\quad+\frac{Z_i}{m_i}\frac{\Delta t}{2}\vec{E}(t)\cdot\nabla\alpha(t),\end{aligned} \tag{19}$$

where $\alpha=\psi,\theta,\zeta$. We note that in Boozer coordinates, the basis vectors are non-orthogonal in nature. However, for

This article is copyrighted as indicated in the article. Reuse of AIP content is subject to the terms at: http://scitation.aip.org/termsconditions. Downloaded to IP: 71.168.238.172 On: Tue, 27 Oct 2015 15:40:32

simplicity, we consider the orthogonal components only, and Eq. (19) can be rewrite as follows:

$$\begin{aligned}
u^{\psi-}(t) = \frac{1}{\mathrm{g}_{\psi\psi}(t)}\Big[& v^{\psi}(t-1/2)\vec{e}_{\psi}(t-1/2)\cdot\vec{e}_{\psi}(t) \\
& + v^{\theta}(t-1/2)\vec{e}_{\theta}(t-1/2)\cdot\vec{e}_{\psi}(t) \\
& + v^{\zeta}(t-1/2)\vec{e}_{\zeta}(t-1/2)\cdot\vec{e}_{\psi}(t)\Big] + \frac{Z_i}{m_i}\frac{\Delta t}{2}\vec{E}(t)\cdot\nabla\psi(t), \\
u^{\theta-}(t) = \frac{1}{\mathrm{g}_{\theta\theta}(t)}\Big[& v^{\psi}(t-1/2)\vec{e}_{\psi}(t-1/2)\cdot\vec{e}_{\theta}(t) \\
& + v^{\theta}(t-1/2)\vec{e}_{\theta}(t-1/2)\cdot\vec{e}_{\theta}(t) \\
& + v^{\zeta}(t-1/2)\vec{e}_{\zeta}(t-1/2)\cdot\vec{e}_{\theta}(t)\Big] + \frac{Z_i}{m_i}\frac{\Delta t}{2}\vec{E}(t)\cdot\nabla\theta(t), \\
u^{\zeta-}(t) = \frac{1}{\mathrm{g}_{\zeta\zeta}(t)}\Big[& v^{\psi}(t-1/2)\vec{e}_{\psi}(t-1/2)\cdot\vec{e}_{\zeta}(t) \\
& + v^{\theta}(t-1/2)\vec{e}_{\theta}(t-1/2)\cdot\vec{e}_{\zeta}(t) \\
& + v^{\zeta}(t-1/2)\vec{e}_{\zeta}(t-1/2)\cdot\vec{e}_{\zeta}(t)\Big] + \frac{Z_i}{m_i}\frac{\Delta t}{2}\vec{E}(t)\cdot\nabla\zeta(t).
\end{aligned} \tag{20}$$

Using Eq. (7), we can simplify the above equations as

$$\begin{aligned}
u^{\psi-}(t) = \frac{(\partial r/\partial\psi)_t}{\mathrm{g}_{\psi\psi}(t)}[& A v^{\psi}(t-1/2)(\partial r/\partial\psi)_{t-1/2} \\
& + B v^{\theta}(t-1/2)r(t-1/2) + C v^{\zeta}(t-1/2) \\
& \times(R_0 + r(t-1/2)\cos\theta(t-1/2))] - \frac{Z_i}{m_i}\frac{\Delta t}{2}\frac{\partial\phi}{\partial\psi}\mathrm{g}^{\psi\psi}, \\
u^{\theta-}(t) = \frac{1}{\mathrm{g}_{\theta\theta}(t)}[& D v^{\psi}(t-1/2)(\partial r/\partial\psi)_{t-1/2}r(t) \\
& + E v^{\theta}(t-1/2)r(t-1/2)r(t) + F v^{\zeta}(t-1/2)r(t) \\
& \times(R_0 + r(t-1/2)\cos\theta(t-1/2))] - \frac{Z_i}{m_i}\frac{\Delta t}{2}\frac{\partial\phi}{\partial\theta}\mathrm{g}^{\theta\theta}, \\
u^{\zeta-}(t) = \frac{1}{\mathrm{g}_{\zeta\zeta}(t)}[& G v^{\psi}(t-1/2)(\partial r/\partial\psi)_{t-1/2} \\
& + H v^{\theta}(t-1/2)r(t-1/2) + P v^{\zeta}(t-1/2) \\
& \times(R_0 + r(t-1/2)\cos\theta(t-1/2))] \\
& \times(R_0 + r(t)\cos\theta(t)) - \frac{Z_i}{m_i}\frac{\Delta t}{2}\frac{\partial\phi}{\partial\zeta}\mathrm{g}^{\zeta\zeta},
\end{aligned} \tag{21}$$

where

$$\begin{aligned}
& A = P\cos\theta_1\cos\theta_2 + \sin\theta_1\sin\theta_2, \\
& B = -P\sin\theta_1\cos\theta_2 + \cos\theta_1\sin\theta_2, \\
& C = \cos\theta_2(-\sin\zeta_1\cos\zeta_2 + \cos\zeta_1\sin\zeta_2), \\
& D = -P\cos\theta_1\sin\theta_2 + \sin\theta_1\cos\theta_2, \\
& E = P\sin\theta_1\sin\theta_2 + \cos\theta_1\cos\theta_2, \\
& F = \sin\theta_2(\sin\zeta_1\cos\zeta_2 - \cos\zeta_1\sin\zeta_2), \\
& G = \cos\theta_1(-\cos\zeta_1\sin\zeta_2 + \sin\zeta_1\cos\zeta_2), \\
& P = \cos\zeta_1\cos\zeta_2 + \sin\zeta_1\sin\zeta_2 \\
& H = -G\tan\theta_1, \theta_1 = \theta(t-1/2), \theta_2 = \theta(t) \\
& \zeta_1 = \zeta(t-1/2), \zeta_2 = \zeta(t).
\end{aligned} \tag{22}$$

In the second step, we consider the rotation of the velocity at time (t). Rotated vector can be written as

$$\vec{u}^{+}(t) = \vec{u}^{-}(t) + \vec{u}^{-}(t)\times\vec{s}(t) + [\vec{u}^{-}(t)\times\vec{T}(t)]\times\vec{s}(t), \tag{23}$$

where $\vec{T} = (Z_i\vec{B}/m_i)(\Delta t/2)$ and $\vec{s} = 2\vec{T}/(1+T^2)$. Most recently, Wei *et al.*,[37] have developed the single particle ion dynamics in general geometry using both toroidal and poloidal components of magnetic field. In our formulations, we also incorporate both toroidal and poloidal components of magnetic fields. However, for the purpose of calculating the ion cyclotron motion in Boris push, we consider the toroidal component of magnetic field only, $\vec{B} = g\nabla\zeta = q\nabla\psi\times\nabla\theta$, and the components of the rotated vector become

$$\begin{aligned}
u^{\psi+}(t) &= \left[1 - \left(\frac{2}{1+T^2}\right)\left(\frac{Z_i}{m_i}\frac{\Delta t}{2}\right)^2 B^2\right]u^{\psi-}(t) \\
&\quad + \left(\frac{2}{1+T^2}\right)\left(\frac{Z_i}{m_i}\frac{\Delta t}{2}\right)\left(\frac{g}{J}\right)\mathrm{g}_{\theta\theta}(t)u^{\theta-}(t), \\
u^{\theta+}(t) &= \left[1 - \left(\frac{2}{1+T^2}\right)\left(\frac{Z_i}{m_i}\frac{\Delta t}{2}\right)^2 B^2\right]u^{\theta-}(t) \\
&\quad - \left(\frac{2}{1+T^2}\right)\left(\frac{Z_i}{m_i}\frac{\Delta t}{2}\right)\left(\frac{g}{J}\right)\mathrm{g}_{\psi\psi}(t)u^{\psi-}(t), \\
u^{\zeta+}(t) &= u^{\zeta-}(t),
\end{aligned} \tag{24}$$

where $T = (Z_iB/m_i)(\Delta t/2)$. We assume orthogonal basis vectors, so that the off-diagonal terms of metric tensor are zero, and one can redefine the Jacobian as $J^2 = \mathrm{g}_{\psi\psi}\mathrm{g}_{\theta\theta}\mathrm{g}_{\zeta\zeta}$, and the diagonal components of the metric tensor as $\mathrm{g}_{\psi\psi} = (\partial r/\partial\psi)^2$, $\mathrm{g}_{\theta\theta} = r^2$, $\mathrm{g}_{\zeta\zeta} = (R_0 + r\cos\theta)^2$. For $g = 1$ and $B = (1 + r/R_0\cos\theta)^{-1}$, one can explicitly prove that

$$\begin{aligned}
& u^{\psi+2}\mathrm{g}_{\psi\psi}(t) + u^{\theta+2}\mathrm{g}_{\theta\theta}(t) + u^{\zeta+2}\mathrm{g}_{\zeta\zeta}(t) \\
& \quad = u^{\psi-2}\mathrm{g}_{\psi\psi}(t) + u^{\theta-2}\mathrm{g}_{\theta\theta}(t) + u^{\zeta-2}\mathrm{g}_{\zeta\zeta}(t),
\end{aligned} \tag{25}$$

i.e., the magnitude of velocity is unchanged during the rotation. In the third step, we add the other half electric acceleration to the rotated vectors to obtain the velocity at time $(t+1/2)$

$$u^{\alpha}(t+1/2) = u^{\alpha+}(t) + \frac{Z_i}{m_i}\frac{\Delta t}{2}\vec{E}(t)\cdot\nabla\alpha(t). \tag{26}$$

To update the particle position, we need to recover $\vec{v}(t+1/2)$, which can be achieved through the following transformation (cf. Fig. 2 dark purple arrow):

$$v^{\gamma}(t+1/2) = \sum_{\alpha=\psi,\theta,\zeta} u^{\alpha}(t+1/2)\vec{e}_{\alpha}(t)\cdot\nabla\gamma(t+1/2), \tag{27}$$

where $\gamma = \psi, \theta, \zeta$. However, the basis vector $\nabla\gamma(t+1/2)$ is still unknown, since $\gamma(t+1/2)$ does not exist in standard leap-frog scheme. Here, we use an estimator for $\gamma(t+1/2)$ as

$$\gamma(t+1/2) = \gamma(t) + u^{\gamma}(t+1/2)\frac{\Delta t}{2}. \tag{28}$$

This article is copyrighted as indicated in the article. Reuse of AIP content is subject to the terms at: http://scitation.aip.org/termsconditions. Downloaded to IP: 71.168.238.172 On: Tue, 27 Oct 2015 15:40:32

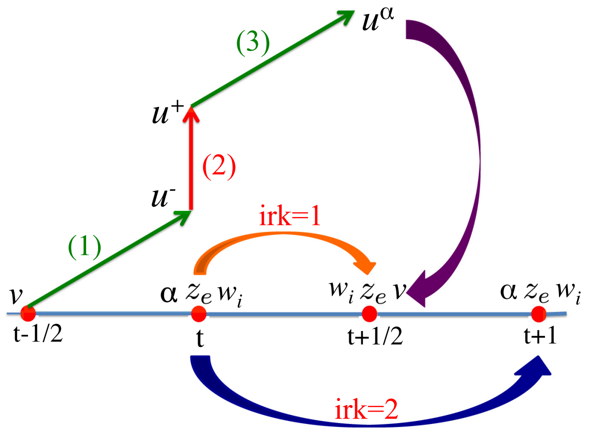

FIG. 2. Schematic diagram for the PIC cycle and ion Boris push. The first step indicates the addition of the first half of the electric field acceleration to the velocity ($v \to u^-$). The second step is rotation of the velocity vector ($u^- \to u^+$). In the third step, we add the second half of the electric field impulse to the rotated velocity component ($u^+ \to u^\alpha, \alpha = \psi, \theta, \zeta$). Ion particle weight ($w_i$) and electron guiding center (z_e) are updated using the second order Runge-Kutta (irk = 1 and irk = 2) method. Dark purple blue indicates the transformation from $u^\alpha \to v$, which is needed to update the ion position [cf. Eq. (27)].

After we find the velocity at time $(t + 1/2)$, we can update the particle position using the leap-frog scheme as

$$\gamma(t+1) = \gamma(t) + v^\gamma(t+1/2)\Delta t. \tag{29}$$

In Eq. (27), we have the dot-product of two basis vectors at different time steps. We have evaluated this equation in a similar way as described in Eqs. (20)–(22).

To verify this cyclotron integrator, we have carried out a single particle ion dynamics in toroidal geometry with inverse aspect ratio $r/R_0 = 0.357$ and $\rho_i/r = 0.0048$. First, we calculate the time variations of the poloidal flux function and the poloidal angle in the absence of electric field [cf. Fig. 3 green line]. Second, we introduce a radial electric field in the particle equation of motion. In the presence of this static electric field, an ion will experience a $\vec{E} \times \vec{B}$ drift in the poloidal direction, as shown in Fig. 3 (magenta line).

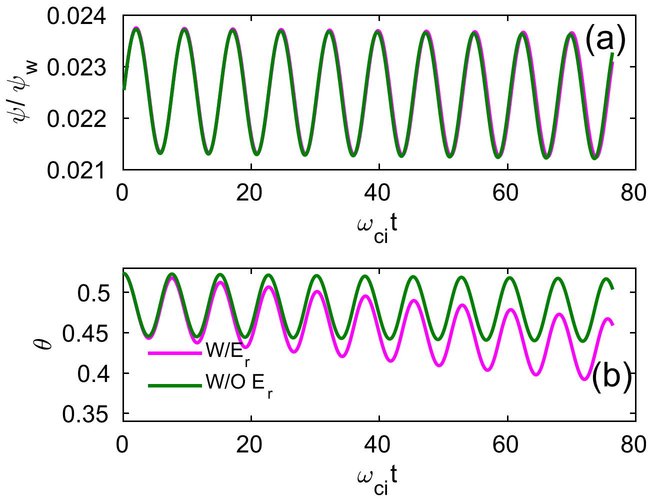

FIG. 3. Verification of $\vec{E} \times \vec{B}$ drift in toroidal geometry. Time variations of (a) poloidal flux function and (b) poloidal angle of the ion position. Here, ψ_w is the poloidal flux function at the last closed flux surface.

TABLE I. Comparison of ion cyclotron motion including $\vec{E} \times \vec{B}$ drift from simulation and theory.

Parameter	Theory	GTC simulation
Gyro radius	8.415×10^{-3} (m)	8.46×10^{-3} (m)
Gyro frequency	4.557×10^{6} (rad/s)	4.538×10^{6} (rad/s)
$\vec{E} \times \vec{B}$ drift	1.815×10^{4} (m/s)	1.785×10^{4} (m/s)

These results between the theory and GTC simulations are summarized in Table I.

Figs. 4(a) and 4(b) present the time step convergence of the poloidal flux function and the relative energy error of the marker particle. Fig. 4(a) demonstrates that poloidal flux function can converge with 40 time steps per cyclotron period ($\omega_{ci}\Delta t = 0.153$). However, there is no such time dependent relation for the calculation of the energy error. Error in the energy arises mostly due to the decomposition of velocity during the first and last steps of the Boris scheme and is within the acceptable limit ($\sim 10^{-5}$).

We have discussed the time advancement of the dynamical quantities such as velocity and position of ion in the time centered manner. However, for the self-consistent simulation, we need to update particle weight, electron guiding center, and electric field. We use the second order RK method to advance these quantities, which is described in Section II C. In our global simulation, we use reflective boundary conditions for the particle and fields.

C. RK pusher for particle weight and electron dynamics

Using the initial ion velocity at time $(t - 1/2)$, the ion particle push module updates the velocity up to (t + 1/2). The velocity at time (t) is computed by the linear average of velocities as follows:

$$v^\gamma(t) = \frac{v^\gamma(t-1/2) + v^\gamma(t+1/2)}{2}. \tag{30}$$

Using the electric field and average velocity at time (t), one can compute (dw_i/dt) from Eq. (10). For the first step of the RK method, we advance the particle weight from $w_i(t)$ to $w_i(t + 1/2)$, and $w_e(t)$ to $w_e(t + 1/2)$. With the updated values of the source term (charge density), the field solver computes the electric field at time $(t + 1/2)$ (cf. Fig. 2 orange arrow). In the second step of RK, we use the updated electric field at $(t + 1/2)$ for the advancement of the particle weight and electron guiding center (z_e) from (t) to $(t + 1)$ [cf. Fig. 2 dark blue arrow]. Mathematically, we can write these two steps as follows:

■ First step (irk = 1)

▶ Ion pusher $\to w_i(t+1/2) = w_i(t) + \left.\frac{dw_i}{dt}\right|_t \frac{\Delta t}{2}$,

▶ Electron pusher $\Rightarrow \begin{cases} z_e(t+1/2) = z_e(t) + \left.\frac{dz_e}{dt}\right|_t \frac{\Delta t}{2} \\ w_e(t+1/2) = w_e(t) + \left.\frac{dw_e}{dt}\right|_t \frac{\Delta t}{2} \end{cases}$

- Solve field solver for $\vec{E}(t+1/2)$.

This article is copyrighted as indicated in the article. Reuse of AIP content is subject to the terms at: http://scitation.aip.org/termsconditions. Downloaded to IP: 71.168.238.172 On: Tue, 27 Oct 2015 15:40:32

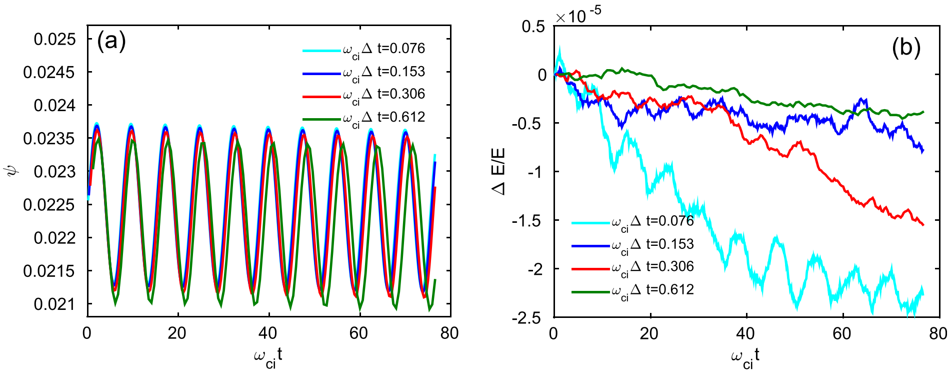

FIG. 4. Time step convergence of (a) poloidal flux function and (b) relative energy error of ion.

■ Second step (irk = 2)

► Ion pusher → $w_i(t+1) = w_i(t) + \left.\frac{dw_i}{dt}\right|_{(t+1/2)} \Delta t,$

$$\blacktriangleright \text{Electronpusher} \Rightarrow \begin{cases} z_e(t+1) = z_e(t) + \left.\frac{dz_e}{dt}\right|_{(t+1/2)} \Delta t \\ w_e(t+1) = w_e(t) + \left.\frac{dw_e}{dt}\right|_{(t+1/2)} \Delta t \end{cases}$$

- Solve field solver for $\vec{E}(t+1)$.

III. LINEAR VERIFICATION OF NORMAL MODES AND NONLINEAR PARTICLE TRAPPING

In this section, we will discuss the electrostatic normal modes with $k_\parallel = 0$ as a benchmark of toroidal Boris scheme in the linear simulation. The general dispersion relation of the normal mode in uniform plasma can be written as[23]

$$1 + \chi_j = 0. \tag{31}$$

For a Maxwellian background, one can write down the susceptibility as

$$\chi_j = -\sum_{j=e,i} \frac{1}{k^2 \lambda_{Dj}^2} \sum_{l=1}^{\infty} \frac{2l^2 \omega_{cj}^2}{\omega^2 - l^2 \omega_{cj}^2} I_l(b_j) e^{-b_j}, \tag{32}$$

where $b_j = k_\perp^2 \rho_j^2$, $\rho_j = \sqrt{(T_j/m_j)}/\omega_{cj}$, $\lambda_{Dj}^2 = \epsilon_0 T_j / n_{0j} e^2$, and $\omega_{ci} = Z_i B/m_i$. For normal modes (LHW, IBW), we have $|\omega/\omega_{ce}| \sim \mathcal{O}(\omega/\omega_{ce}) \ll 1$ and $k_\perp \rho_e \ll 1$, hence the electron susceptibility is dominated by $l = 1$ term. Therefore, the above Eq. (32) becomes

$$1 + \frac{\omega_{pe}^2}{\omega_{ce}^2} - \frac{1}{k_\perp^2 \lambda_{Di}^2} \sum_{l=1}^{\infty} \frac{2l^2 \omega_{ci}^2}{\omega^2 - l^2 \omega_{ci}^2} I_l(b_i) e^{-bi} = 0. \tag{33}$$

For long wavelength limit $k \to 0^+$, with $\omega_{ci} \ll \omega \ll \omega_{ce}$, the frequency of the LHW is

$$\omega_{LH}^2 = \omega_{pi}^2 \left(1 + \frac{\omega_p^2}{\omega_c^2}\right)^{-1}. \tag{34}$$

We use an artificial antenna to excite these modes and to verify the mode structure and frequency in our simulation. The electrostatic potential of the antenna can be written as

$$\phi_{ext} = \phi_0 \sin(k_r r) \cos(\omega_0 t) \cos(m_0 \theta - n_0 \zeta). \tag{35}$$

In our simulation, the inverse aspect ratio of the tokamak is $r/R_0 = 0.018$, $\rho_i/r = 0.002$, and the background plasma density is uniform with a uniform temperature. We use poloidal and toroidal mode filters to select m = 0, n = 0 modes. For the lower hybrid simulation, $\omega_{pi} = 145.2\omega_{ci}$, $\omega_{pe} = 6242.8\omega_{ci}$,$\omega_{ci}\Delta t \simeq 1.33 \times 10^{-3}$, $m_e/m_i = 5.44618 \times 10^{-4}$, and particles per wavelength are 8×10^6. We carry out the scan with different antenna frequencies and determine the frequency in which the mode response has the maximum growth of the amplitude. This frequency is then identified as the eigenmode frequency of the system. Fig. 5(a) presents the time history of the lower hybrid wave amplitude for the antenna frequency $\omega_0 = 41.0\omega_{ci}$, which agrees well with the analytical frequency $40.9\omega_{ci}$. Also, the amplitude of the LHW increases linearly with time, since there is no damping due to $k_\parallel = 0$. To avoid the boundary effects, we consider $(\Delta/\rho_i = 41.13)$, where Δ is the width of the simulation domain.

Similarly, we carried out the simulation of the IBW waves for the first four harmonics $(l = 1 - 4)$. In this simulation by changing the plasma density, we consider $\omega_{pi} = 10.01\omega_{ci}$, $\omega_{pe} = 422.3\omega_{ci}$, $\Delta/\rho_i = 19.45$, $\omega_{ci}\Delta t \simeq 0.055$, and particles per wavelength are 8×10^6. Fig. 5(b) shows good agreement between the analytical and GTC simulation results of the IBW frequency. For a definitive comparison between GTC simulation and analytical theory, we have restricted our simulation to the core of the plasmas $r/a = 0.018$. The magnetic field variation in this region is less than 2% since the local analytical theory uses a uniform magnetic field.

As the first step in developing this nonlinear toroidal particle simulation model, we carry out the nonlinear GTC simulation of electron trapping by the LHW with a large amplitude [cf. Fig. 6] in cylindrical geometry. Initially, the linear lower hybrid eigen mode $(m = 4$ and $n = 1)$ is excited using an artificial antenna. After the wave amplitude reaches the plateau regime, we turn off the antenna, and the wave decays exponentially due to the Landau damping on electrons in the linear simulation (blue line).[30] The linear damping rates obtained from the theory $(0.32\omega_{LH})$ agree well with the simulation $(0.31\omega_{LH})$. However, in the nonlinear simulation, the resonant electrons can be trapped by the electric field of the wave. The wave amplitude becomes oscillatory with a frequency equal to the trapped electron oscillation frequency (magenta line). The bounce frequencies $\omega_b =$

This article is copyrighted as indicated in the article. Reuse of AIP content is subject to the terms at: http://scitation.aip.org/termsconditions. Downloaded to IP: 71.168.238.172 On: Tue, 27 Oct 2015 15:40:32

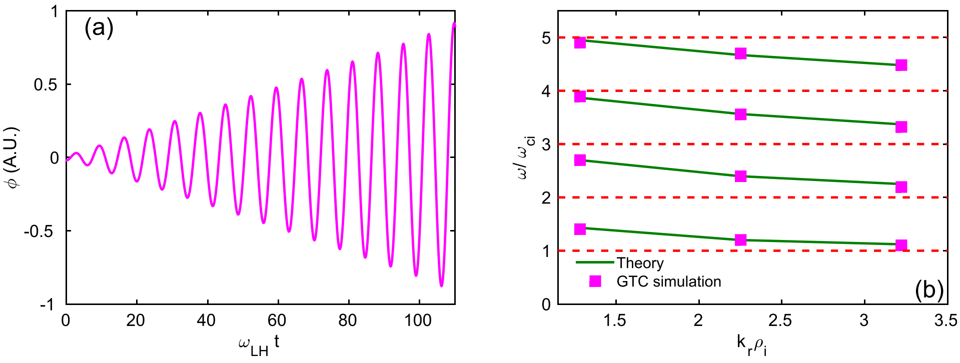

FIG. 5. Verification of normal modes in toroidal geometry. (a) Time history of LHW amplitude excited by antenna, (b) comparison of IBW dispersion relation between the analytical solution and the GTC simulations for the first four harmonics.

$k_{\parallel} v_{the} \sqrt{e\phi/T_e}$ are close to the analytical values (Table II). During the antenna excitation of LHW eigenmode, the particle dynamics are linear for both linear and nonlinear simulation.

IV. PDI OF ION CYCLOTRON WAVE AND NONLINEAR ION HEATING

Magnetized plasma supports a large number of electrostatic and electromagnetic modes. When wave energy is relatively low, these modes are mutually independent and represent a description for the response of the plasma to local perturbation and external field. However, at higher amplitudes, these modes are coupled and exchange momentum and energy with each other through the coherent wave phenomenon, e.g., PDIs. In this process, the pump wave $(\omega_0, \vec{k}_0)$ decays into two daughter waves or one daughter wave $(\omega_1, \vec{k}_1)$ and a quasimode $(\omega_2, \vec{k}_2)$ pair. The selection rule for this decay process is given by

$$\omega_0 = \omega_1 + \omega_2 \qquad \vec{k}_0 = \vec{k}_1 + \vec{k}_2. \tag{36}$$

As demonstrated in Figure 7, the pump wave can decay into one daughter wave with a near zero wavenumber and another wave with nearly the same wavenumber as the pump wave. This process is considered to be the most probable non-resonant decay channel of PDI in the ion cyclotron heating regime. Possible decay channels in the ion cyclotron range of frequency (ICRF) in experiments have been discussed by Porkolab.[45] In Figure 7, we show the IBW dispersion relation (green lines) for the same parameter as in Figure 5(b). In our simulation, the pump wave itself is not an IBW, and the value of ω/ω_{ci} at the antenna position is 2.25, as indicated in Fig. 7. When $\omega_0 = \omega_{\rm IBW} + \omega_{ci}$, i.e., the frequency shift of the wave is close to the ion cyclotron frequency, the wave is strongly damped on ions and known as ICQM.

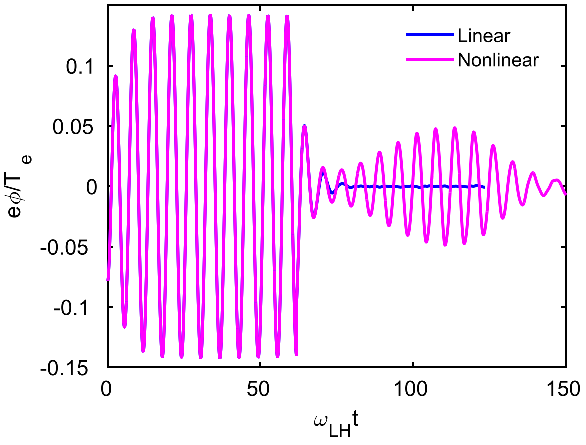

FIG. 6. Nonlinear GTC simulation of LHW exhibits oscillation in wave amplitude (magenta line), while linear simulation shows exponential decay (blue line).

Under experimental conditions, a pump wave of fixed frequency passing through the nonuniform plasma density and temperature experiences the variation of the wave vector to satisfy the dispersion relation. As a result of this inhomogeneity, layers may exist where selection rules of mode-mode coupling are easily satisfied. However, in our simulation, plasma density and temperature are uniform and the wave vectors of the pump wave and the sideband wave are chosen by the antenna. To satisfy the frequency matching condition in our simulation, we scan the pump wave frequencies with fixed wavevector. The energy transfer from the wave to ion (nonlinear ion heating) is maximal, when the frequency selection of parametric decay, $\omega_1 = \omega_{\rm IBW}$, and $\omega_2 = \omega_{ci}$ are satisfied (cf. Fig. 8(a) red line). Otherwise, the energy transfer is negligible (cf. Fig. 8(a) green and blue lines). Our simulations are all electrostatic and we choose the wave vector in the radial direction only $(i.e., k_{\parallel} = 0)$ for both pump wave and decay waves. We consider $\omega_{pi} = 10.01\omega_{ci}$, $\omega_{pe} = 422.3\omega_{ci}$, $\Delta/\rho_i = 19.45$, 100 radial grid points per wavelength, 200 particles per cell. The simulation time step $(\omega_{ci}\Delta t \simeq 0.02)$ is sufficient to resolve IBW, ion cyclotron wave, and pump wave dynamics. In this case, the particles trajectory is described by the perturbed electric field in addition to the equilibrium magnetic field [cf. Section II A]. Fig. 8(b) shows that the temperature of the hot ions increases linearly as the amount of rf power increases, since the kinetic energy of the ion $[(1/2)m_i(U/c_s)^2]$ is proportional to $(e\phi/T_i)^2$, where $U/c_s = k_{0\perp}\rho_i(e\phi/T_i)$ is the normalized ion velocity and $c_s = \sqrt{T_e/m_i}$ is the ion sound speed. We measure the energy of the ion after 400 ion cyclotron periods.

TABLE II. Comparison of bounce frequency of nonlinearly trapped particle in LHW simulation.

$e\phi/T_e$	Theory	GTC simulation
0.00885	$2.91\omega_{ci}$	$3.04\omega_{ci}$
0.04866	$6.8\omega_{ci}$	$6.7\omega_{ci}$

This article is copyrighted as indicated in the article. Reuse of AIP content is subject to the terms at: http://scitation.aip.org/termsconditions. Downloaded to IP: 71.168.238.172 On: Tue, 27 Oct 2015 15:40:32

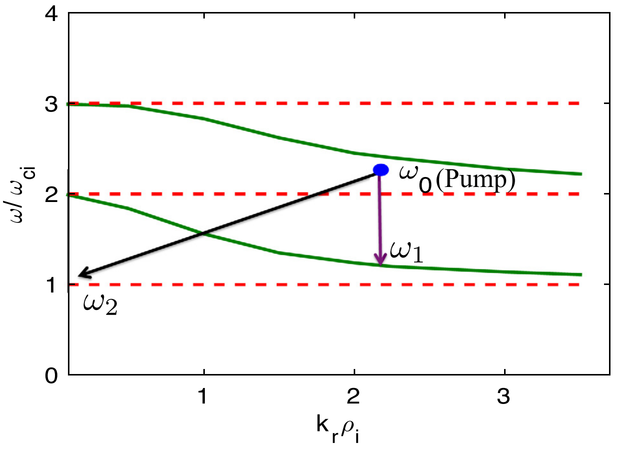

FIG. 7. Schematic of an IBW parametric decay process. Pump wave $(\omega_0, \vec{k}_0)$ decays into an IBW side band $(\omega_1, \vec{k}_1)$ and an ion cyclotron quasi mode (ICQM) $(\omega_2, \vec{k}_2)$. Green lines represent the theoretical dispersion curve of the IBW for first two harmonics.

This simulation time is long enough to excite the daughter waves for the prominent PDI phenomenon. All channels of PDI require certain threshold power to overcome the losses due to linear damping and convection of the decay waves out of the region of interaction. There is no convective loss in the current simulation since the pump wave amplitude is uniform. The threshold power for the instability due to the linear damping of the decay waves is given by $\gamma_0^2 = \gamma_L \gamma_{L1}$, where γ_L and γ_{L1} are the linear damping rates of the ICQM and IBW sideband, respectively. However, in our simulation, the linear damping of the decay waves is zero, since the parallel wave vectors are zero.

Fig. 9 shows that ion heating takes place only in the perpendicular direction. The ion temperature in the parallel direction does not change. Since the wave heating predominantly affects the perpendicular ion distribution, which is consistent with the results observed in the scrape-off layer (SOL) of DIII-D,[13] Alcator-C Mod,[14] and HT-7[15] experiments during the IBW heating and high harmonic fast waves heating in NSTX.[16] This parasitic absorption of the wave energy degrades the efficiency of ion Bernstein and ion cyclotron harmonics resonance heating. However, our simulations are limited to the core region only. In our nonlinear simulation, the ponderomotive effect is absent, since we consider the plasma response in the r direction only. With the present simulation setup, the amount of power transferred to the plasma has not been measured directly. During the linear simulation, wave particle interaction can be possible only through the linear damping, which is negligible compared to the nonresonant damping.

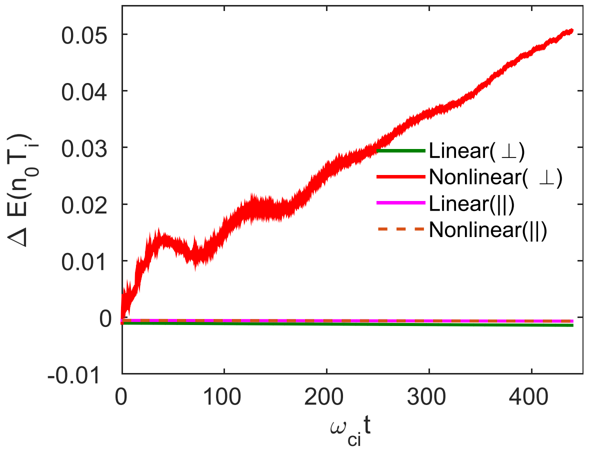

FIG. 9. Time history of change of kinetic energy of ion. Green and magenta lines represent the energy change during linear simulation in the perpendicular and parallel directions, respectively. Red and dotted lines indicate the energy change during nonlinear simulation in the perpendicular and parallel direction, respectively.

V. DISCUSSION

In summary, nonlinear global toroidal particle simulations have been developed using fully kinetic ion and drift kinetic electron to study the electron trapping by LHW and parametric decay process of ICRF waves in uniform core plasma. We verify our simulation results with the linear dispersion relation. In the nonlinear simulation of LHW, we find that the amplitude of the electrostatic potential oscillates with a bounce frequency, which is due to the wave trapping of resonant electrons. We also find nonlinear anisotropic ion heating due to nonresonant three wave coupling. One must mention here that in a tokamak scenario with non-uniform density and temperature, the energy density of the wave can begin to approach the thermal energy in the edge. Since, in the edge region the densities and temperatures are factors of 10^2 to 10^3 lower than in the core, produce strong ponderomotive effects

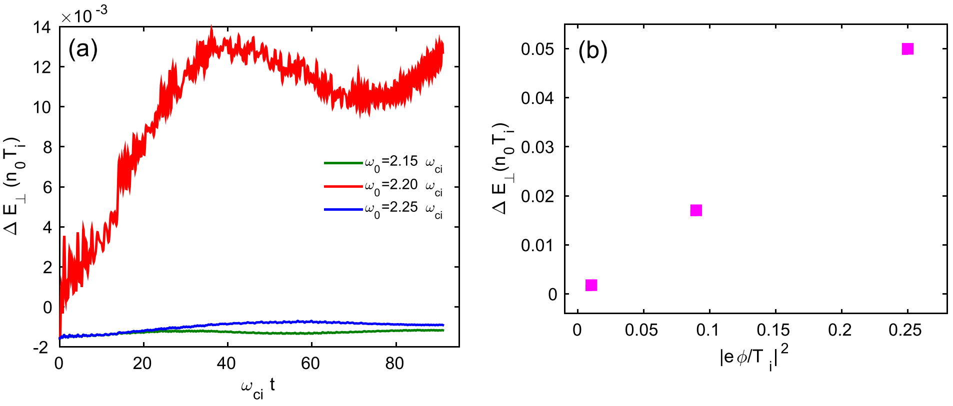

FIG. 8. (a) Time history of change of perpendicular kinetic energy of ion for different pump wave frequency and (b) change in kinetic energy of ion as a function of intensity of the pump wave.

This article is copyrighted as indicated in the article. Reuse of AIP content is subject to the terms at: http://scitation.aip.org/termsconditions. Downloaded to IP: 71.168.238.172 On: Tue, 27 Oct 2015 15:40:32

and parametric decay physics. It must be noted that we have not done such realistic simulations. The simulation region and the number of tests are restricted due to limited computational resources in this paper.

ACKNOWLEDGMENTS

A.K. would like to thank Dr. R. B. White for his useful suggestions. This work was supported by PPPL Subcontract No. S013849-F, U.S. Department of Energy (DOE) SciDAC GSEP Program and China National Magnetic Confinement Fusion Energy Research Program, Grant Nos. 2013GB111000 and 2015GB110003. Simulations were performed using the super computer resources of the Oak Ridge Leadership Computing Facility at Oak Ridge National Laboratory (DOE Contract No. DE-AC05-00OR22725) and the National Energy Research Scientific Computing Center (DOE Contract No. DE-AC02-05CH11231).

[1] N. J. Fisch, Phys. Rev. Lett. **41**, 873 (1978).
[2] N. J. Fisch, Rev. Mod. Phys. **59**, 175 (1987).
[3] C. Gormezano, A. C. C. Sips, T. C. Luce, S. Ide, A. Becoulet, A. Litaudon, A. Isayama, J. Hobrik, M. R. Wade, T. Oikawa, R. Prater, A. Zvonkov, B. Llyod, T. Suzuki, E. Barbato, P. Bonoli, C. K. Phillips, V. Vdovin, E. Joffrin, T. Casper, J. Ferron, D. Mazon, D. Moreau, R. Bundy, C. Kessel, A. Fukuyama, N. Hayashi, F. Imbeaux, M. Murakami, A. R. Polevoi, and H. E. StJohn, Nucl. Fusion **47**, S285 (2007).
[4] ITER Physics Expert Group on Energetic Particles Heating and Drive, Current and Editors, ITER Physics Basis, Nucl. Fusion **39**, 2495 (1999).
[5] ITER website http://www.iter.org.
[6] E. F. Jaeger, L. A. Berry, E. DAzevedo, D. B. Batchelor, and M. D. Carter, Phys. Plasmas **8**, 1573 (2001).
[7] M. Brambilla, Plasma Phys. Controlled Fusion **41**, 1 (1999).
[8] Y. Peysson, J. Decker, and L. Morini, Plasma Phys. Controlled Fusion **54**, 045003 (2012).
[9] P. Bonoli, IEEE Trans. Plasma Sci. **12**, 95 (1984).
[10] S. G. Baek, R. R. Parker, S. Shiraiwa, G. M. Wallace, P. T. Bonoli, D. Brunner, I. C. Faust, A. E. Hubbard, B. LaBombard, and M. Porkolab, Plasma Phys. Controlled Fusion **55**, 052001 (2013).
[11] R. Cesario, L. Amicucci, C. Castaldo, M. Kempenaars, S. Jachmich, J. Mailloux, O. Tudisco, A. Galli, A. Krivska, and JET-EFDA Contributors, Plasma Phys. Controlled Fusion **53**, 085011 (2011).
[12] R. Cesario, L. Amicucci, A. Cardinali, C. Castaldo, M. Marinucci, L. Panaccione, F. Santini, O. Tudisco, M. L. Apicella, G. Calabro, C. Cianfarani, D. Frigione, A. Galli, G. Mazzitelli, C. Mazzotta, V. Pericoli, G. Schettini, A. A. Tuccillo, and FTU Team, Nat. Commun. **1**, 55 (2010).
[13] R. Pinsker, C. Petty, M. Mayberry, M. Porkolab, and W. Heidbrink, Nucl. Fusion **33**, 777 (1993).
[14] J. C. Rost, M. Porkolab, and R. L. Boivin, Phys. Plasmas **9**, 1262 (2002).
[15] J. Li, Y. Bao, Y. P. Zhao, J. R. Luo, B. N. Wan, X. Gao, J. K. Xie, Y. X. Wan, and K. Toi, Plasma Phys. Controlled Fusion **43**, 1227 (2001).
[16] T. M. Biewer, R. E. Bell, S. J. Diem, C. K. Phillips, J. R. Wilson, and P. M. Ryan, Phys. Plasmas **12**, 056108 (2005).
[17] V. Pericoli-Ridolfini, R. Bartiromo, A. Tuccillo, F. Leuterer, F.-X. Soldner, K.-H. Steuer, and S. Bernabei, Nucl. Fusion **32**, 286 (1992).
[18] T. Fujii, M. Saigusa, H. Kimura, M. Ono, K. Tobita, M. Nemoto, Y. Kusama, M. Seki, S. Moriyama, T. Nishitani, H. Nakamura, H. Takeuchi, K. Annoh, S. Shinozaki, and M. Terakado, Fusion Eng. Des. **12**, 139 (1990).
[19] M. H. Li, B. J. Ding, J. Z. Zhang, K. F. Gan, H. Q. Wang, Y. Peysson, J. Decker, L. Zhang, W. Wei, Y. C. Li, Z. G. Wu, W. D. Ma, H. Jia, M. Chen, Y. Yang, J. Q. Feng, M. Wang, H. D. Xu, J. F. Shan, F. K. Liu, and EAST Team, Phys. Plasmas **21**, 062510 (2014).
[20] A. Kuley and V. K. Tripathi, Phys. Plasmas **16**, 032504 (2009).
[21] A. Kuley and V. K. Tripathi, Phys. Plasmas **17**, 062507 (2010).
[22] A. Kuley, C. S. Liu, and V. K. Tripathi, Phys. Plasmas **17**, 072506 (2010).
[23] C. S. Liu and V. K. Tripathi, Phys. Rep. **130**, 143 (1986).
[24] L. Qi, X. Y. Wang, and Y. Lin, Phys. Plasmas **20**, 062107 (2013).
[25] T. G. Jenkins, T. M. Austin, D. N. Smithe, J. Loverich, and A. H. Hakim, Phys. Plasmas **20**, 012116 (2013).
[26] C. Gan, N. Xiang, J. Ou, and Z. Yu, Nucl. Fusion **55**, 063002 (2015).
[27] Z. Yu and H. Qin, Phys. Plasmas **16**, 032507 (2009).
[28] Z. Lin, T. S. Hahm, W. W. Lee, W. M. Tang, and R. B. White, Science **281**, 1835 (1998).
[29] A. Kuley, Z. X. Wang, Z. Lin, and F. Wessel, Phys. Plasmas **20**, 102515 (2013).
[30] J. Bao, Z. Lin, A. Kuley, and Z. X. Lu, Plasma Phys. Controlled Fusion **56**, 095020 (2014).
[31] W. Zhang, Z. Lin, and L. Chen, Phys. Rev. Lett. **101**, 095001 (2008).
[32] H. S. Zhang, Z. Lin, and I. Holod, Phys. Rev. Lett. **109**, 025001 (2012).
[33] Z. Wang, Z. Lin, I. Holod, W. W. Heidbrink, B. Tobias, M. Van Zeeland, and M. E. Austin, Phys. Rev. Lett. **111**, 145003 (2013).
[34] Y. Xiao and Z. Lin, Phys. Rev. Lett. **103**, 085004 (2009).
[35] J. McClenaghan, Z. Lin, I. Holod, W. Deng, and Z. Wang, Phys. Plasmas **21**, 122519 (2014).
[36] D. Liu, W. Zhang, J. McClenaghan, J. Wang, and Z. Lin, Phys. Plasmas **21**, 122520 (2014).
[37] X. S. Wei, Y. Xiao, A. Kuley, and Z. Lin, Phys. Plasmas **22**, 092502 (2015).
[38] J. Bao, Z. Lin, A. Kuley, and Z. X. Wang, "Electromagnetic particle simulation model for nonlinear processes of lower hybrid waves in fusion plasmas" Phys. Plasma (submitted).
[39] J. Bao, Z. Lin, A. Kuley, and Z. X. Wang, "Electromagnetic particle simulation of toroidal effects on linear mode conversion and absorption of lower hybrid waves" Nucl. Fusion (submitted).
[40] R. B. White and M. S. Chance, Phys. Fluids **27**, 2455 (1984).
[41] Y. Xiao, I. Holod, Z. Wang, Z. Lin, and T. Zhang, Phys. Plasmas **22**, 022516 (2015).
[42] J. Boris, in *Proceedings of the Fourth International Conference on Numerical Simulation of Plasmas* (NRL, 1970), p. 367.
[43] C. K. Birdsall and A. B. Langdon, *Plasma Physics via Computer Simulation* (Institute of Physics, New York, 2005).
[44] A. J. Brizard and T. S. Hahm, Rev. Mod. Phys. **79**, 421 (2007).
[45] M. Porkolab, Fusion Eng. Des. **12**, 93 (1990).

This article is copyrighted as indicated in the article. Reuse of AIP content is subject to the terms at: http://scitation.aip.org/termsconditions. Downloaded to IP: 71.168.238.172 On: Tue, 27 Oct 2015 15:40:32